Global Biogeochemical Cycles

RESEARCH ARTICLE
10.1029/2018GB005905

A Detailed View on the Seasonality of Stable Carbon Isotopes Across the North Atlantic

Meike Becker[1,2,3], Tobias Steinhoff[3], and Arne Körtzinger[3,4]

[1]Geophysical Institute, University of Bergen, Bergen, Norway, [2]Bjerknes Centre for Climate Research, Bergen, Norway, [3]GEOMAR Helmholtz Centre for Ocean Research Kiel, Chemical Oceanography, Kiel, Germany, [4]Christian Albrecht University, Sektion Chemie, Kiel, Germany

Key Points:
- Three years of continuous underway measurements of stable carbon isotopes in sea surface CO_2 were performed in the North Atlantic Ocean
- A cavity ringdown spectrometer was successfully implemented and operated autonomously on a commercial vessel
- The isotope signature of air-sea gas exchange was determined

Supporting Information:
- Supporting Information S1
- Data Set S1

Correspondence to:
M. Becker,
meike.becker@uib.no

Citation:
Becker, M., Steinhoff, T., & Körtzinger, A. (2018). A detailed view on the seasonality of stable carbon isotopes across the North Atlantic. *Global Biogeochemical Cycles*, *32*, 1406–1419. https://doi.org/10.1029/2018GB005905

Received 20 FEB 2018
Accepted 17 AUG 2018
Accepted article online 26 AUG 2018
Published online 28 SEP 2018

©2018. The Authors.
This is an open access article under the terms of the Creative Commons Attribution-NonCommercial-NoDerivs License, which permits use and distribution in any medium, provided the original work is properly cited, the use is non-commercial and no modifications or adaptations are made.

Abstract The North Atlantic Ocean plays a major role in climate change not the least due to its importance in CO_2 uptake and thus natural carbon sequestration. The CO_2 concentration in its surface waters, which determines the ocean's CO_2 sink/source function, varies on seasonal and interannual time scales and is mainly driven by air-sea gas exchange, temperature variability, and biological production/respiration. The variability in stable carbon isotope signatures can provide further insight and help to improve the understanding of the controls of the surface ocean carbon system. In this work, a cavity ringdown spectrometer was coupled to a classical, equilibrator-based pCO_2 system on a voluntary observing ship line that regularly sails across the subpolar North Atlantic between North America and Europe. From 2012 to 2014, a 3-year time series of underway surface $\delta^{13}C(CO_2)$ data was obtained along with continuous measurements of temperature, salinity, and fCO_2. We perform a decomposition of thermal and nonthermal drivers of fCO_2 and $\delta^{13}C(CO_2)$. The direct measurement of the surface ocean $\delta^{13}C(CO_2)$ allows us to estimate the mass flux and also the stable carbon isotope fractionation during air-sea gas exchange. While the CO_2 mass flow was in the range of 1–2 mol $CO_2 \cdot m^{-2} \cdot year^{-1}$ on the shelves and 2.5–3.5 mol $CO_2 \cdot m^{-2} \cdot year^{-1}$ in the open ocean, the isotope signature of this CO_2 flux with respect to the sea surface ranged from -2.6 ± 1.4‰ on the shelves to -6.6 ± 0.9‰ in the western and -4.5 ± 0.9‰ in the eastern part of the open ocean section.

1. Introduction

The ocean surface is the window through which the anthropogenic carbon signal enters the interior ocean. The world's oceans take up about one quarter of the annual anthropogenic CO_2 emissions from fossil fuel burning. Cumulatively, they have taken up nearly 40% of all fossil fuel CO_2 emissions since 1750 (Le Quéré et al., 2018). During the past 30 years, substantial progress has been made in observing the variability of the fugacity of CO_2 (fCO_2) in the surface ocean and estimating the ocean carbon sink by performing extensive underway measurements on board voluntary observing ships (VOSs). The anthropogenically induced change is visible not only in rising concentrations of CO_2 but also in the stable carbon isotope ratio in the atmosphere changes. The combustion of fossil fuels, which are of biological origin and therefore depleted in ^{13}C with respect to their carbon source (Lloyd & Farquhar, 1994), leads to a lightening (i.e., a depletion in ^{13}C and hence a reduction in the $^{13}C/^{12}C$ ratio) of the stable carbon pool in atmosphere and ocean, the so-called ^{13}C Suess effect. In several studies, the oceanic Suess effect has been used to estimate the distribution of anthropogenic carbon in the oceans (Gruber et al., 2002; Körtzinger et al., 2003; Olsen et al., 2006; Quay et al., 2017; Racapé et al., 2013). Most processes influencing the Earth's carbon system also come with a change in isotopic composition, a process which is called fractionation. We can distinguish between equilibrium fractionation (e.g., between the inorganic carbon species in thermodynamic equilibrium) and kinetic fractionation (e.g., most biologically mediated processes). These fractionations alter the isotope composition of both, the substrate, and the product. The stable carbon isotope ratio of a sample is usually expressed relative to a standard material (V-PDB, Vienna Pee Dee Belemnite) in per mil (Friedman et al., 1982).

$$\delta^{13}C = \left(\frac{R_{sample}}{R_{V-PDB}} - 1 \right) \cdot 1{,}000 \quad (1)$$

with R_{sample} and R_{V-PDB} being the ratio of C^{13} to C^{12} in the respective substance.

Generally, the distribution of carbon isotopes is a useful tool to track changes within the Earth's carbon system.

Many processes that alter the carbon concentration, such as primary production or air-sea gas exchange, alter also the stable isotope composition in a specific way. Therefore, biological processes such as primary production or respiration have a different fingerprint as physical processes, which leads to another very useful application, that is, separating this process from physical mixing and estimating net community production (Quay et al., 2009; Quay & Wu, 2015).

On longer time scales, the uptake of anthropogenic carbon will mainly be dependent on the transport rate of surface water into the interior ocean and the extent to which this water is equilibrated with the atmosphere. Therefore, the ocean surface is a key area to study for tracking anthropogenic carbon in the atmosphere and in the ocean using stable carbon isotopes. Variations in the isotopic disequilibrium will directly influence the estimate of how much carbon is stored in the ocean.

One major limitation of a more widespread use of isotope data lies in the significant effort involved in their collection and the resulting scarce number of available data. Up to now, the isotopic air-sea disequilibrium was calculated from δ^{13}C(DIC) measured on discrete seawater samples and the fractionation between the total dissolved inorganic CO_2 (DIC) species and gaseous CO_2. Through temperature- and salinity-dependent fractionation an error is introduced to the disequilibrium determined this way. Continuous wave cavity ringdown spectroscopy (CRDS), a relatively novel technology that has recently been introduced into environmental research, now provides the possibility of precise and continuous isotope ratio measurements. This development of highly precise spectroscopic methods for the simultaneous determination of ^{12}C and ^{13}C mole fractions in gaseous CO_2 made it possible to measure the isotopic disequilibrium directly. Moreover, these analyzers are robust enough to be coupled to an equilibrator-based pCO_2 system on a ship, providing continuous data of the ocean surface and thus a coverage and resolution in time and space, which had not been achievable previously (Becker et al., 2012). Especially when installing such a system on a VOS, the seasonal and, in a longer perspective, also the interannual variability in the isotope signature of the CO_2 flux can be measured. This isotope information in addition to the fCO_2 measurements gives us the opportunity to learn more about which processes drive the variability in the surface ocean carbon system. Which role do biological processes play? How large is the influence of temperature? And how do these two influence the isotopic disequilibrium with the atmosphere and thus the progression of the anthropogenic signal from the atmosphere into the surface ocean.

In this study, we present a 3-year time series of combined surface ocean fCO_2 and $\delta^{13}C(CO_2)$ data, measured on board a VOS across the North Atlantic. Based on this, we determine the mass flux and its isotopic signature between ocean and atmosphere in its seasonal variability as well as its annual mean. For understanding the variability in the isotope ratio of the air-sea flux, we perform a decomposition of drivers of the $\delta^{13}C(CO_2)$ seasonality into thermally and biologically (i.e., nonthermally) driven components.

2. Data and Methods

The studied region, the North Atlantic between 40°N and 60°N, shows both subpolar and subtropical influences. The southwestern part is characterized by more subtropical warm and salty waters of the Gulf Stream (GS), which are transported northward along the American coast and finally flow eastward to the open ocean. The GS shows a significant meandering that changes from a single branch to multiple fronts once it reaches the Grand Banks. Here it meets the western boundary current of the subpolar gyre, the Labrador Current (LC), which transports cold and relatively fresh water out of the Labrador Sea. At any time of the year cold, cyclonic eddies at the seaward side of the front and warm, anticyclonic eddies on the shoreside can be observed, making this a very energetic and highly variable region (Frankignoul et al., 2001). After mixing with the LC the GS flows northeastward, forming the North Atlantic Current and then continuing as the North Atlantic Drift Current. East of 12°W, the water shows clear coastal influences as most of this region is already located on the European shelf.

The vessel used in this study, the hybrid container roll-on/roll-off vessel M/V Atlantic Companion, was sailing between Liverpool, UK, and Halifax, Canada. Whether the vessel followed a route north or south of Ireland was dependent on the location of the major atmospheric low pressure systems and did not show a seasonal pattern. Near the western boundary of the sampling area, the vessel sailed significantly further south in late spring/early summer caused by the more southward extent of the ice border at that time of the year. An overview of the transects used in this study can be found in Table A1 in Appendix A. One transect lasted usually around 6 days.

2.1. Underway Setup

The data used in this study were measured in the years 2012 to 2014 by combining a commercially available CRDS analyzer (G2131-*i*, Picarro, USA) with a commercial autonomous pCO_2 system as described in Pierrot et al. (2009) and Steinhoff et al. (2010). This setup was installed in the engine room of M/V Atlantic Companion. The water inlet was located about 250 m astern of the ship's forecastle at a water depth of 9.6–10.6 m, about 2 m away from the pCO_2 system. Caused by variations in the draught of the vessel, the water intake was at deeper water depth during westbound transects than during eastbound transects. However, this did not have a traceable effect on the measurements. Sea surface temperature (SST) and sea surface salinity (SSS) were measured by an external intake temperature sensor (SBE-38) and a thermosalinograph (SBE-21, both Sea-Bird Inc, USA), respectively. The CRDS system was installed in the flow of seawater-equilibrated air downstream of the nondispersive infrared CO_2 detector (LI-COR Inc., USA) of the pCO_2 system via a bypass (Becker et al., 2012). The gas flow out of the CRDS was recombined with the main gas flow and redirected to the equilibrator. The CRDS pump was specially sealed to avoid any ambient air to leak into the loop. During crossings without CRDS measurements, the LI-COR was calibrated every 3 hr by using three nonzero calibration gases. The CRDS was calibrated every 8 hr with two calibration gases. The fCO_2 data were processed according to U.S. Department of Energy guidelines (Dickson et al., 2007).

2.2. Data Reduction and Accuracy of the CRDS Data

The CRDS data were calibrated by using two calibration gases with different $\delta^{13}C(CO_2)$ values as well as different CO_2 mixing ratios. The CO_2 concentration of these gases was determined by calibration against National Oceanic and Atmospheric Administration (NOAA) primary standards using the CRDS analyzer. The isotope ratio by calibration against standardized reference material using an isotope ratio mass spectrometer (calibrated at the Laboratory for Stable Isotope Mass Spectrometry, Heidelberg, Germany). Since the calculation routine of the CRDS analyzer uses absorption peak heights instead of area integrals to determine the concentrations of the respective species, the instrument output is dependent on the composition of the analyzed gas, which influences the pressure broadening of the absorption line. For seawater, variable oxygen content is the main driver of changes in the gas composition and hence absorption line shape. The instrument output was corrected for varying oxygen mole fractions with an instrument-specific relation of xO_2 and the pressure broadening parameter y after Friedrichs et al. (2010) and Becker et al. (2012).

The $\delta^{13}C(CO_2)$ was then corrected to SST by using the temperature-dependent fractionation to DIC after Zhang et al. (1995):

$$\delta^{13}C\left(CO_2\right)_{SST} = \delta^{13}C\left(CO_2\right)_{EQU} - 0.107\left(T_{EQU} - T_{SST}\right) + 0.014\left(T_{EQU}\frac{[CO_3^{2-}]_{EQU}}{[DIC]_{EQU}} - T_{SST}\frac{[CO_3^{2-}]_{SST}}{[DIC]_{SST}}\right) \quad (2)$$

with T_{EQU} and T_{SST} as the equilibrator and SST, $[CO_3^{2-}]_{EQU}$ and $[CO_3^{2-}]_{SST}$ the concentration of carbonate ions, and $[DIC]_{EQU}$ and $[DIC]_{SST}$ the DIC concentration, calculated at the respective temperatures.

Finally, a centered moving average filter with a length of about 15 min was applied to the isotope ratio data in order to reduce the statistical noise of the analyzer. The chosen averaging time of 15 min is a compromise between improving the instruments precision by applying longer averaging times and still capturing observed gradients and natural variations that happen on a time scale shorter than the optimal averaging time of 150 min. This compromise was determined by comparing different averaging times on data from an intense bloom event. Here the chosen averaging time did improve the data precision significantly but did not mask features that were resolved with shorter averaging times.

The accuracy of the fCO_2 measurements is estimated to be 2 µatm for seawater. This sums up uncertainties stemming from the nondispersive infrared gas analyzer and the equilibration process, as well as pressure and temperature difference between the equilibrator and the surface water (Pierrot et al., 2009). For the $\delta^{13}C(CO_2)$ measurements the accuracy is estimated to be on the order of 0.15‰.

2.3. Samples

Discrete samples for DIC and total alkalinity (TA) were taken on selected cruises from the water supply line about every 6 hr between 10°W and 55°W. Assuming an average vessel speed of 25-30 km/h this relates to a spatial resolution of about 150–200 km between two samples. The samples were taken following the Depart-

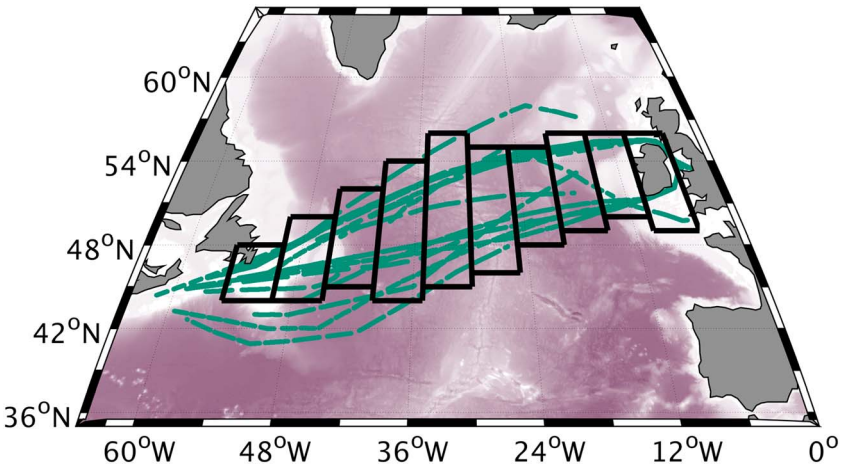

Figure 1. Vessel tracks with observations and the meridional bands that were used in this study.

ment of Energy guidelines (Dickson et al., 2007). A 500-ml sample was poisoned with 100-µl saturated mercury chloride solution and then stored dark until analysis in the laboratory in Kiel. A Single-Operator Multiparameter Metabolic Analyzer (SOMMA) system was used for DIC, and a Versatile INstrument for the Determination of Titration Alkalinity system (VINDTA) was used for TA measurements (Johnson et al., 1993, 1998; Mintrop et al., 2000). The accuracy of the DIC and TA samples was assured by regular CRM measurements, and the precision was estimated using duplicate samples and resulted in 2.9 µmol/kg for DIC and 5.1 µmol/kg for TA.

2.4. Calculation of DIC and δ^{13}C(DIC)

Continuous alkalinity data matching the CO_2 and $\delta^{13}C(CO_2)$ measurements were calculated using the following alkalinity-salinity correlation, which is based on the discrete TA samples taken from the VOS line during the period January 2012 to December 2014 and covering all seasons. ($n = 277$).

$$TA = 738 + 43 \times SSS + 0.057 \times SSS^2 + 0.1205 \times t - 3.46 \times 10^{-4} \times t^2 \quad (3)$$

with SSS being the sea surface salinity, t the day of the year, and TA the total alkalinity in µmol/kg. The mean difference ± the standard deviation between the measured and the calculated alkalinity is (0 ± 12)µmol/kg. Using this alkalinity, the DIC was calculated from the fCO_2 data via CO2SYS (van Heuven et al., 2009; CO_2 dissociation constants from Mehrbach et al., 1973, and KSO_4^- dissociation constants from Dickson & Millero, 1987), resulting in a good agreement with the DIC samples of (3±7) µmol/kg (calculated DIC − measured DIC).

The isotope ratio of DIC was calculated from $\delta^{13}C(CO_2)_{EQU}$ using the fractionation factor ϵ_{CO_2-DIC} reported in Zhang et al. (1995). This conversion adds an additional uncertainty to the isotope data of about 0.15‰.

2.5. Harmonic Fits

All data were averaged into meridional bands with a longitudinal width of 5° (Figure 1). The latitudinal extend of these bands was chosen to include the normal sailing route of the vessel. Data from further north or south than 1σ of the mean latitude of each band were excluded. In the western part, the bands cover both subtropical and subpolar water masses. Since this is a highly energetic mixing region, in which we found strong eddies containing both subtropical and subpolar waters, but also different mixing states of both end members, we decided to not separate the two water masses and show the observed variability in this region instead.

For every band, the seasonality was fitted using a harmonic fit function according to Zeng et al. (2002),

$$\chi = c_0 + c_1 \sin\left(\frac{2\pi t}{365}\right) + c_2 \cos\left(\frac{2\pi t}{365}\right) + c_3 \sin\left(\frac{4\pi t}{365}\right) + c_4 \cos\left(\frac{4\pi t}{365}\right), \quad (4)$$

$$\chi = c_0 + c_1 \sin\left(\frac{2\pi t}{365}\right) + c_2 \cos\left(\frac{2\pi t}{365}\right) + c_3 \sin\left(\frac{4\pi t}{365}\right), \quad (5)$$

where t is the day of year and c_0 to c_4 the respective fitting parameters. Most parameters were fitted using equation (4). Equation (5) was used for fitting the fCO_2 and its disequilibrium with the atmosphere (ΔfCO_2) since it offered a better description of the observed variability.

2.6. Decomposition of Driving Factors

The temperature-driven and the non-temperature-driven components of the fCO_2 ($fCO_2@T_{obs}$ and $fCO_2@T_{mean}$) were calculated after Takahashi et al., 1993 (1993; equations (6) and (7)). Since the stable carbon isotope ratio of DIC as a conservative property is constant with temperature, the decomposition of $\delta^{13}C(CO_2)$ can be based on the temperature-dependent fractionation between DIC and CO_2 (equations (8) and (9)).

$$fCO_2@T_{obs} = fCO_{2,mean} \cdot \exp\{0.0423\left(T_{mean} - T_{obs}\right)\}, \tag{6}$$

$$fCO_2@T_{mean} = fCO_{2,obs} \cdot \exp\{0.0423\left(T_{obs} - T_{mean}\right)\}, \tag{7}$$

$$\begin{aligned}\delta^{13}C\left(CO_2\right)@T_{obs} =& \delta^{13}C\left(CO_2\right)_{mean} - 0.107\left(T_{mean} - T_{obs}\right)\\ &+0.014\left(T_{mean}\frac{[CO_3^{2-}]_{mean}}{[DIC]_{mean}} - T_{obs}\frac{[CO_3^{2-}]_{obs}}{[DIC]_{obs}}\right),\end{aligned} \tag{8}$$

$$\begin{aligned}\delta^{13}C\left(CO_2\right)@T_{mean} =& \delta^{13}C\left(CO_2\right)_{obs} - 0.107\left(T_{obs} - T_{mean}\right)\\ &+0.014\left(T_{obs}\frac{[CO_3^{2-}]_{obs}}{[DIC]_{obs}} - T_{mean}\frac{[CO_3^{2-}]_{mean}}{[DIC]_{mean}}\right).\end{aligned} \tag{9}$$

The subscript *obs* refers to the observed values, while the subscript *mean* refers to the respective annual mean.

2.7. Air-Sea Gas Exchange

The atmospheric fCO_2 ($fCO_{2,ATM}$) and $\delta^{13}C(CO_2)_{ATM}$ were calculated for each meridional band based on time series measurements from atmosphere monitoring stations at Mace Head, Ireland (53.33°N, −9.90°E); Bermuda, UK (32.26°N, −64.88°E); Vestmannaeyjar, Iceland (63.40°N, 20.29°E); and the Azores, Portugal (38.75°N, −27.08°E) between January 2012 and December 2014 (Cooperative Global Atmospheric Data Integration Project, 2015; White et al., 2015). Since the atmospheric CO_2 content shows a strong latitudinal dependence, this dependence was used to calculate the atmospheric xCO_2 and $\delta^{13}C(CO_2)_{ATM}$ over the ocean as a function of latitude and date. All grid points within the respective latitude were averaged to one mean seasonal cycle per band. The $fCO_{2,ATM}$ was calculated from the $xCO_{2,ATM}$ using the harmonic fits of SST, SSS, and air pressure.

Wind speed data were taken from the Modern Era Retrospective-analysis for Research and Applications, version 2, which uses the Goddard Earth Observing System Data Assimilation System, version 5. The barometric pressure as obtained from this reanalysis was in good agreement with our measurements on board. The gas transfer velocity k_{600} was calculated according to Nightingale et al. (2000) for the entire wind field. The gas transfer velocity was then averaged into a daily mean per band, and a 6-day moving average was applied. The actual k at the respective temperatures was calculated using the Schmidt number dependence after Wanninkhof (1992) and the solubility coefficient K_0 according to Weiss (1974).

The sea-to-air flux of total CO_2 (F) and $^{13}CO_2$ (F_{13}) was calculated using equations (10) to (12).

$$F = k \times K_0 \times \left(fCO_{2,SEA} - fCO_{2,ATM}\right), \tag{10}$$

$$F_{13} = \alpha \times k \times K_0 \times \left(\frac{R_{SEA} \times fCO_{2,SEA}}{1 + R_{SEA}} - \frac{R_{ATM} \times fCO_{2,ATM}}{1 + R_{ATM}}\right), \tag{11}$$

$$\epsilon_{ASE} = \left(\frac{F_{13}}{F - F_{13}}/R_{SEA} - 1\right) \times 1{,}000, \tag{12}$$

where K_0 is the solubility of CO_2 in seawater, k the gas transfer velocity, α the fractionation during gas exchange, and R_{SEA} and R_{ATM} the respective stable carbon isotope ratios of CO_2 in seawater and the atmosphere (calculated after equation (1)).

Please note that ϵ_{ASE} describes the isotopic composition of the flux between atmosphere and ocean relative to the isotopic composition of the surface ocean. A negative ϵ_{ASE} means that the gas exchange is lightening

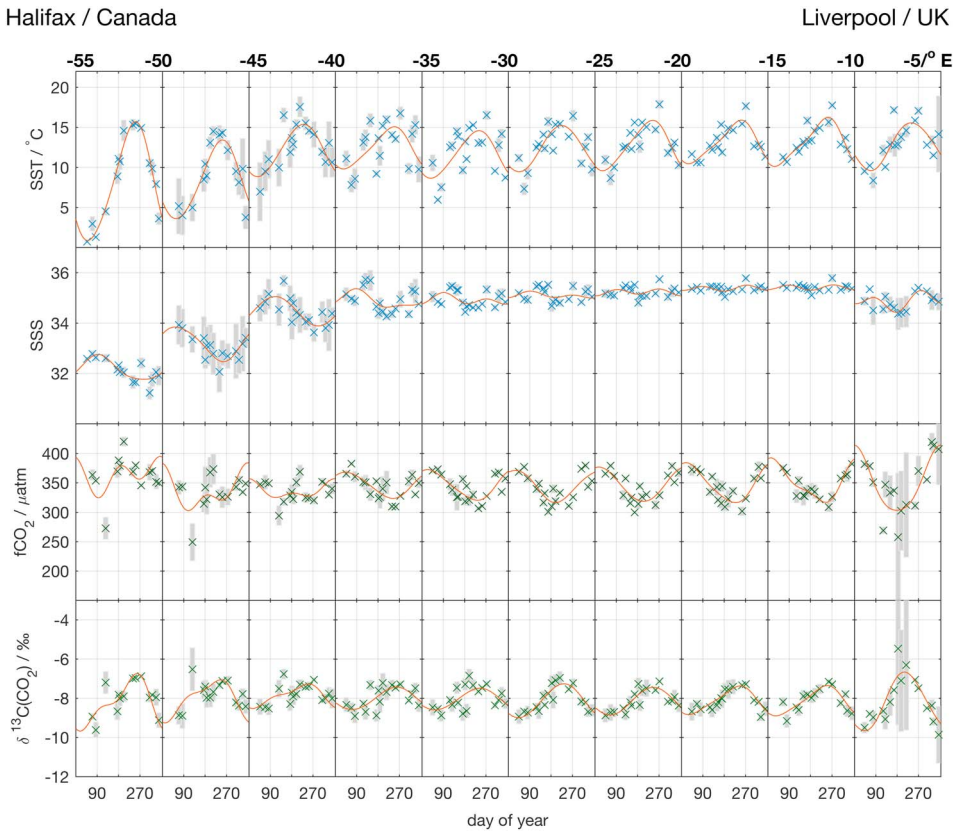

Figure 2. Seasonal variation of SST, SSS, fCO_2, and $\delta^{13}C(CO_2)$ for all 10 bands as measured with autonomous instrumentation installed on our North Atlantic voluntary observing ship line during the period 2012–2014. The crosses show the respective band average for each crossing and the gray boxes show its standard deviation. This contains information about the actual variability in the measured underway data. The harmonic fits are displayed as red lines. The number above the plot refers to the longitudinal borders of the respective bands. SSS = sea surface salinity; SST = sea surface temperature.

the surface ocean DIC during understaturated conditions, but the surface ocean DIC becomes heavier when the mass flux direction changes. As the ϵ_{ASE} is not only dependent on the isotopic disequilibrium but also on the magnitude of the mass flux, it can reach extreme values in case of an isotopic disequilibrium with no net mass flux.

2.8. Estimation of Errors and Uncertainties

For the estimation of errors, every band average was associated with its standard deviation. Using a normal distribution for each band average with these standard deviations as width, a set of harmonic fits was produced with a Monte Carlo approach. The uncertainty of the gas exchange parameterization was estimated to be 20% (Nightingale et al., 2000). The standard deviation of the fluxes resulting from this set of fits was then used as the flux uncertainties. The uncertainty of the fractionation during gas exchange was determined by the standard deviation of the Monte Carlo runs, weighted by the mass flow of this flux. This reduces the otherwise high influence of Monte Carlo runs with small mass flow and, thus, extreme fractionations.

3. Results and Discussion

3.1. Seasonal Cycles

The seasonal cycles of SST, SSS, fCO_2, and $\delta^{13}C(CO_2)$ are shown in Figure 2. The variability during the respective crossings is shown as gray boxes, representing the standard deviation of the respective band mean. In general, it can be stated that the variability is higher in the west than in the east. The SST peak-to-peak amplitude decreases from about 15 °C off Nova Scotia to slightly above 5 °C in the eastern bands. Especially the winter minimum is much lower in the west, which is caused by the influence of cold LC water on the shelf. The salinity is lower in the west, compared to the east. In the mixing region of the relatively fresh water from the LC and

the saline GS water between 35°W and 50°W, high variability was found. In the salinity data, we can observe a small seasonal cycle with higher salinities in late winter and a minimum in fall.

The observed patterns in fCO_2 seasonality across the North Atlantic are well described in the literature (Lüger et al., 2004; Takahashi et al., 2009). The region east of 40°W shows a seasonality that is more typical for subpolar regions. A distinct decrease toward a summer minimum due to primary production is followed by an increase caused by convective mixing in fall and winter. The amplitude is increasing toward the east from about 50 to 80 µatm. The easternmost region, between 5°W and 10°W, is located on the shelf, showing high spatial variability during summer, which can be seen in the high standard deviation of the band averages. Very intense blooms in spring were followed by also intense respiration signals ventilated through the deepening mixed layer depth in the end of summer. In contrast, the western part shows a bimodal pattern that points toward subtropical influences. The data show an early minimum in spring caused by carbon fixation, during which the fCO_2 can easily be reduced to less than 250 µatm, followed by a temperature-driven maximum during the summer months, which decreases again toward fall. These waters at the front of LC and GS and at the shelf edge of the Grand Banks can be very patchy. The further west, the more pronounced is the subtropical pattern. While there is still a maximum in winter around 45°W, the summer maximum dominates west of 50°W.

The seasonality of $\delta^{13}C(CO_2)$ also shows basic differences between east and west. In the eastern half of the North Atlantic, the seasonal cycle of $\delta^{13}C(CO_2)$ is anticorrelated to fCO_2. The carbon pool becomes heavier as light carbon is preferably taken up by phytoplankton during spring bloom, while upward mixing of respiratory carbon depletes in ^{13}C in the inorganic carbon pool again in fall. In the western part, the anticorrelation is less pronounced and the $\delta^{13}C(CO_2)$ seasonality has two maxima, one during spring bloom and one in late summer. At the frontal region of LC and GS, this enrichment in ^{13}C can lead to $\delta^{13}C(CO_2)$ values higher than −4‰ that are usually not observed in the open ocean, correlated to the extraordinarily low fCO_2 observed in that area.

3.2. Decomposition of Temperature and Nontemperature Effects

Since fCO_2 has a strong temperature dependence, it is often decomposed into a temperature-dependent and non-temperature-dependent component (Takahashi et al., 1993). Note that this decomposition assumes no air-sea exchange of CO_2. This assumption is not strictly valid but generally justified as the CO_2 equilibration time scale of the surface ocean (1 year) is long to the time scales of the seasonal cyles of temperature and net community production. For the data set presented here, this analysis is shown in the upper two panels of Figure 3. The temperature-driven part, fCO_2 @ T_{obs}, shows a minimum in winter and a maximum in summer, with an amplitude decreasing from west to east. This effect is caused by the temperature-dependent solubility of CO_2. The non-temperature-driven part of the fCO_2 seasonality, fCO_2 @ T_{mean}, has an opposite shape. This part contains biological effects: convection and advection. In the temperate North Atlantic, the balance of primary production and respiration is a major driver of fCO_2. The onset of primary production in spring draws down the fCO_2 @ T_{mean}, while the upward mixing of carbon-rich water during fall leads to increasing fCO_2 @ T_{mean}. The amplitude of fCO_2 @ T_{mean} is slightly higher on the shelves, especially in the west, where more intense primary production takes place but does not show a clear longitudinal trend. As a result of this, both components, fCO_2 @ T_{mean} and fCO_2 @ T_{obs}, are of similar magnitude in the western bands, while the non-temperature-driven part is dominating in the east, manifesting the eastward transition from subtropical to more subpolar character of the surface ocean dynamics.

When looking at the decomposition of the seasonality of stable carbon isotope ratios, the main difference to that of the fCO_2 seasonality is that both forcings have the same direction in their effect on $\delta^{13}C(CO_2)$. $\delta^{13}C(CO_2)$ @ T_{obs} shows a summer maximum and winter minimum with an amplitude of 1.5‰ in the west, decreasing to about 1‰ in the eastern part. This variability results from the temperature-dependent equilibrium fractionation within the inorganic carbon system. At higher temperatures the fractionation between CO_2 and the DIC pool is reduced, leading to higher isotope ratios in the measured CO_2 (about 2‰ per 10 °C [Zhang et al., 1995]). The non-temperature-driven part of the $\delta^{13}C(CO_2)$ seasonality ($\delta^{13}C(CO_2)$ @ T_{mean}) shows more variability. Generally, during carbon fixation by phytoplankton the lighter isotopomer is preferred due to kinetic fractionation. This results in an enrichment of the heavier isotopomer in the remaining carbon pool in the surface ocean. During respiration, most of the light biomass is remineralized completely, so that the isotope ratio of inorganic carbon decreases again when remineralized carbon and nutrients are mixed to the surface during convective mixing. East of 35°W the $\delta^{13}C(CO_2)$ @ T_{mean} seasonality shows an amplitude of about 1‰ in the open ocean and a larger amplitude in the shelf. West of 35°W, bimodal patterns are observed. The early

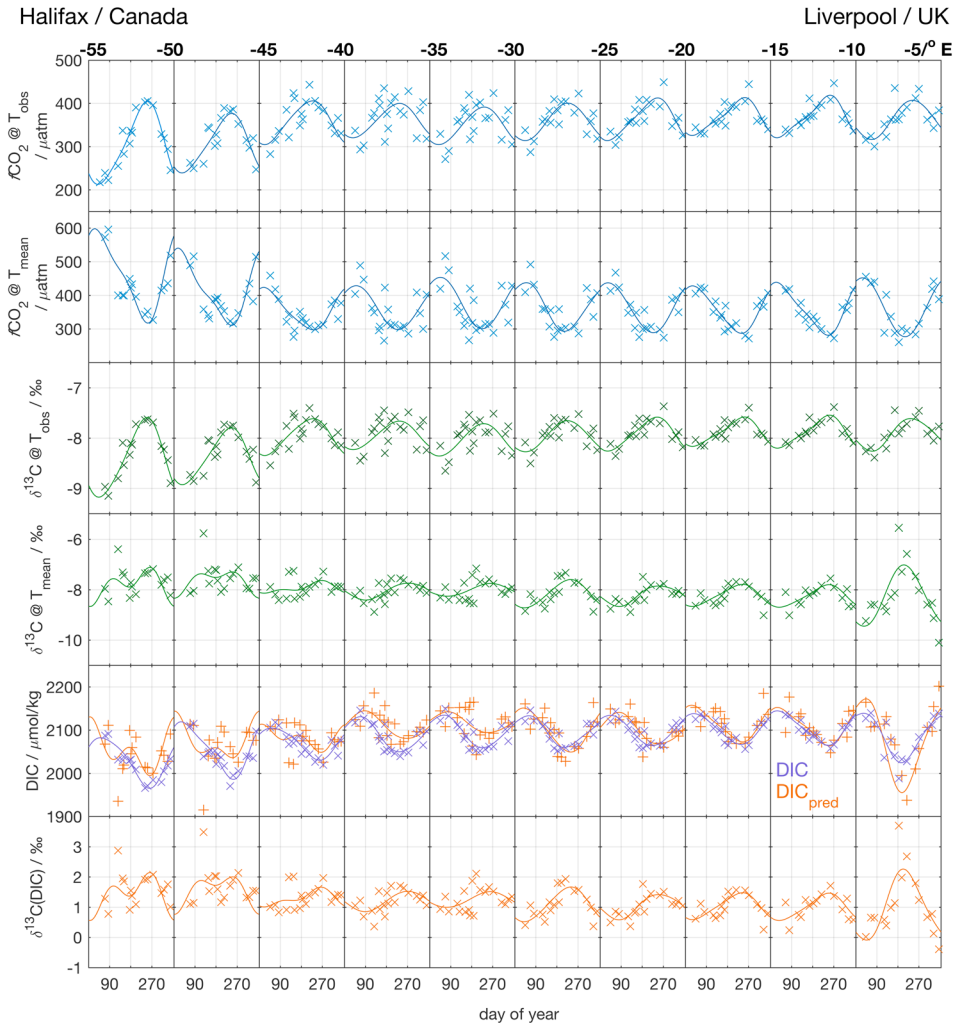

Figure 3. Seasonal variation of the temperature-driven and non-temperature-driven components of fCO_2 and $\delta^{13}C(CO_2)$ as well as of the observed DIC (purple) and the DIC predicted from the $\delta^{13}C(DIC)$ seasonality (red) band $\delta^{13}C(DIC)$ for all 10 bands as measured with autonomous instrumentation installed on our North Atlantic voluntary observing ship line during the period 2012–2014. Each cross refers to the averaged data of one crossing. The lines show a harmonic fit of these band means. The number above the plot refers to the longitudinal borders of the respective bands. DIC = dissolved inorganic CO_2.

and intense spring blooms cause the CO_2 pool to become very heavy in spring, after which the values come back to winter values. A second, smaller increase in the isotope ratio can then be observed in fall.

Another approach to assess the non-temperature-driven variability is the analysis of DIC and $\delta^{13}C(DIC)$ (Figure 3). In order to analyze the impact of primary production/respiration on the DIC concentration, the predicted DIC concentration (DIC_{pred}) was calculated from the winter DIC concentration and the variations in $\delta^{13}C(DIC)$ assuming a fractionation to the produced biomass of −24‰ (Young et al., 2013):

$$DIC_{pred} = \left(\frac{R_{SEA}/1{,}000 + 1}{R_{winter}/1{,}000 + 1} \right)^{\frac{1{,}000}{-24}} \cdot DIC_{winter}, \tag{13}$$

where R_{SEA} is the measured isotope ratio of DIC and R_{winter} and DIC_{winter} are the average DIC concentration and isotope ratio from January to March.

The amplitude in DIC concentration is increasing from east to west with maximal DIC concentrations in late winter caused by entrainment of high DIC subsurface waters and decreases toward a summer minimum as soon as the removal of DIC by net primary production exceeds the entrainment flux. The amplitude as well as the absolute $\delta^{13}C(DIC)$ are also increasing from east to west, showing the same characteristics as

the non-temperature-driven component of the $\delta^{13}C(CO_2)$. In the eastern open ocean bands (10–30°W), it is clearly anticorrelated to the changes in DIC concentration. The amplitude in DIC concentration is about 80 μmol/kg, while that in $\delta^{13}C(DIC)$ shows about 1‰.

The predicted DIC concentration based on the assumption that only primary production and respiration drive the seasonal DIC variability shows a very similar amplitude and timing as the actually measured DIC concentration. So both the DIC and $\delta^{13}C(DIC)$ changes are almost completely biologically driven. This fits well with other studies in the subpolar North Atlantic (Gruber et al., 1999; Racapé et al., 2014). The easternmost band, which is located around the coast of Ireland, shows a larger but still anticorrelated amplitude in both DIC concentration and its stable isotope composition (120 μmol/kg, 2‰). The predicted DIC variations based on the $\delta^{13}C(DIC)$ seasonality show a larger amplitude than the actually measured DIC concentration. This leads to the conclusion that there must be a different source of DIC, for example, fluxes from land or the seafloor, which most likely also carry an isotope composition different to that of surface ocean DIC or phytoplankton biomass.

The picture in the western bands is more complicated, however. The decrease in DIC starts earlier and is steeper in the western part of the basin, while the net entrainment flux starts later in the season as in the eastern open ocean regions. The minimal DIC concentration is reached in August. In these bands the harmonic fit performs not very well in capturing the first steep decline in DIC concentration/increase in $\delta^{13}C(DIC)$, but when looking at the measured values themselves, it becomes visible that the first decrease in DIC in spring bloom of about 80 μmol/kg happens within only 50 days in March/April, associated with an increase in $\delta^{13}C(DIC)$ of 2‰.

This region is known to show a nitrate-depleted conditions from June to August (Steinhoff et al., 2010). The $\delta^{13}C(DIC)$ shows a bimodal structure with one maximum at the time of the first steep DIC drawdown under nitrate-repleted conditions in spring and a second maximum coinciding with the DIC minimum in late summer. This behavior can be explained by two different processes. This region is characterized by oligotrophic conditions and very shallow mixed layer depths during summer. In spring, the available nutrients are used up during a short but intense bloom phase, leading to the first maximum in $\delta^{13}C(DIC)$. The lower $\delta^{13}C$ after the end of spring bloom could be caused by the ingassing of lighter atmospheric carbon, which can have a large influence on surface layer $\delta^{13}C(DIC)$ during shallow mixed layer conditions. A different process that could introduce light carbon into the surface ocean is remineralization. Especially, if this remineralization is not occurring quantitatively in the surface layer, light carbon would be released in the surface layer due to this partial remineralization, while the remaining, relatively heavy particles would sink out of the mixed layer. Khim et al. (2018) found heavier sinking particles during the highly productive seasons. Usually, this is connected to changes in the $\delta^{13}C$ of dissolved CO_2 but in a region with a high rate of remineralized production and a shallow mixed layer as the western part of the area studied here is during summer, a partial remineralization as source of light carbon needs to be considered. The further DIC decrease toward the overall minimum coincides with a decrease in salinity at the same time of the year and the onset of mixed layer deepening in fall. This decrease is coming with an increase in $\delta^{13}C(DIC)$, showing a biological signature (about 0.5‰ per 40 μmol/kg decrease in DIC). As the decrease in DIC is associated with a lower salinity, this signature must be caused by mixing with lower salinity water, which comes with a different isotopic signature and which has experienced a DIC decrease caused by a phytoplankton bloom. The decrease in salinity is a seasonal signature that occurs simultaneously with the onset of convective mixing. Since the MLD in this region is very shallow during summer, evaporation could increase the salinity in the surface layer, so that mixed layer deepening can cause a decrease in salinity. Additionally, increased precipitation during fall would lead to a decrease in salinity. After the cessation of the spring bloom there can be a significant amount of primary production occurring underneath the very shallow mixed layer where the nutrient concentration is not yet fully depleted and light level still permit net primary production. Mixing with this shallow subsurface water mass that is not influenced by air sea gas exchange could provide persistent primary production signal in the $\delta^{13}C(DIC)$. Subsurface blooms in midsummer with a deep chlorophyll maximum are reported for subtropical regions and consume nutrients near the nutricline below the shallow summer mixed layer. This scenario is consistent with the delay of a net entrainment flux of nutrients relative to the onset of deepening of the mixed layer and can explain the observed pattern. Another process that could possibly cause such a signature would be a fall bloom that produces the biological isotope signature and coincides with lateral mixing of lower salinity waters that were influenced by ice melting in summer.

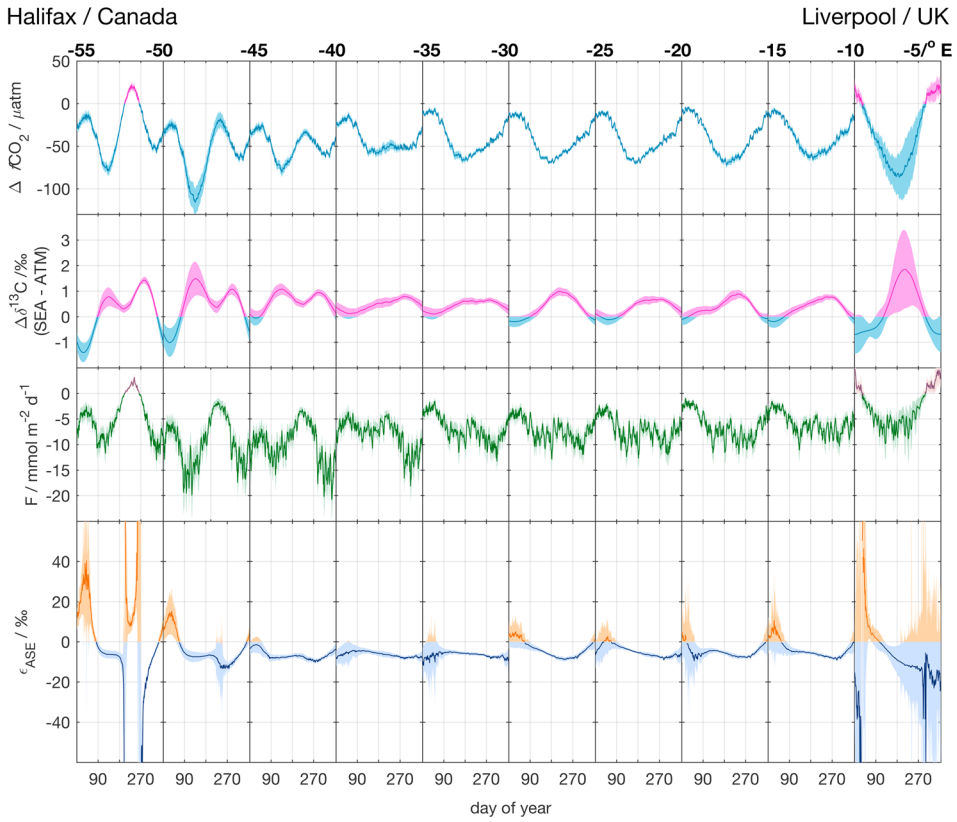

Figure 4. Seasonal variation of the air-sea disequilibria in CO_2 partial pressure and carbon isotope signature, the estimated air-sea gas exchange fluxes of total CO_2, and the stable carbon isotope signature of this flux for all 10 bands as measured with autonomous instrumentation installed on our North Atlantic voluntary observing ship line during the period 2012–2014. The colored areas cover the uncertainty as the standard deviation of the Monte Carlo runs. The number above the plot refers to the longitudinal borders of respective bands.

3.3. Air-Sea Gas Exchange

The shape of the seasonality of the CO_2 air-sea disequilibrium (ΔfCO_2) is in agreement with previous studies of Lüger et al. (2004) and Takahashi et al. (2009; Figure 4). In the eastern and central open ocean regions, the fCO_2 is close to atmospheric equilibrium in winter and shows an undersaturation of about 60–70 µatm during summer. This undersaturation is caused by net carbon fixation during the spring bloom as discussed above. The increase in inorganic carbon due to deepening mixed layer depths in fall and winter brings the fCO_2 again close to the atmospheric fCO_2 as a major fraction of the organic carbon exported over the summer period is remineralized above the maximum winter mixed layer depth and thus returned to the atmosphere (Körtzinger et al., 2008). On the shelf, this leads to supersaturated conditions in winter as less organic carbon can be exported to the deep ocean via cross-shelf export. In the seasonal cycle of ΔfCO_2 in the western part of the basin we observe again a bimodal pattern, in which the temperature-driven fCO_2 maximum in summer causes supersaturation. A combination of cooling and the occurrence of a fall bloom triggered by upwelled nutrients, causes then an air-sea disequilibrium during winter.

The isotopic disequilibrium with the atmosphere is mostly driven by the combination of temperature changes and biological effects, discussed above for the $\delta^{13}C(CO_2)$ seasonality. In contrast to fCO_2, the impacts of these two drivers are in phase, resulting in a heavy CO_2 pool during summer. During winter the inorganic carbon in the open ocean regions is not only nearly in mass equilibrium but also in isotopic equilibrium with the atmosphere. This can be explained by the circumstance that the surface ocean on the North Atlantic is relatively close to atmospheric equilibrium as the water has already been traveling northward for many years. Under these conditions the summer bloom generates only a transient perturbation. Moreover, the cooling of the water as it is leaving the subtropical gyre toward the subpolar North Atlantic reduces the isotopic disequilibrium. Toward the shelves, the more intense respiration and cooling signals cause the inorganic carbon in the

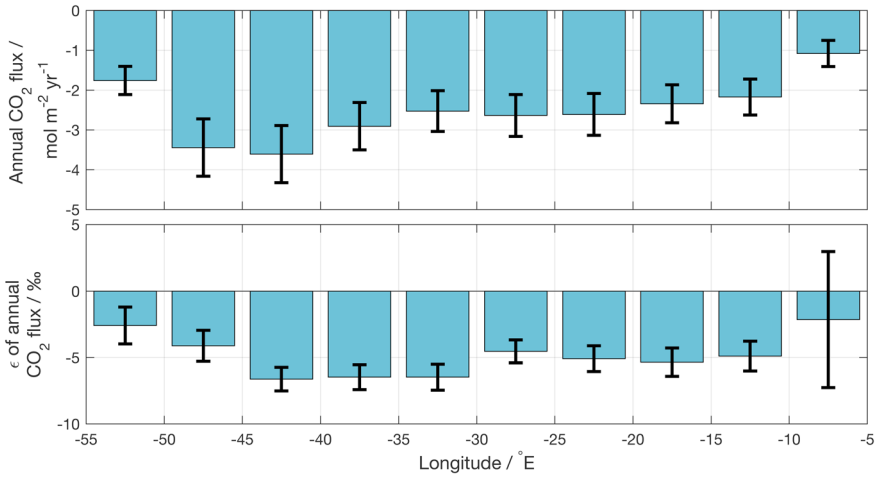

Figure 5. Average annual net air-sea flux (upper panel) and its stable carbon isotope composition (lower panel) for all 10 bands as measured with autonomous instrumentation installed on our North Atlantic voluntary observing ship line during the period 2012–2014.

surface ocean to be lighter than the atmospheric CO_2. During summer, the inorganic carbon in the surface ocean is everywhere up to 2‰ heavier than the atmosphere. In intense bloom patches this disequilibrium can be much larger.

The fluxes in total CO_2 and $^{13}CO_2$ as well as the stable carbon isotope ratio of this flux, ϵ_{ASE}, are shown in the lower panels of Figure 4. In the eastern part, the air-sea flux is small during the winter due to the small concentration gradient between atmosphere and ocean. In summer this concentration difference is larger and hence also the air-sea flux. In the western part, the picture is again more diverse. Here we observe the largest fluxes during spring and late fall, when the disequilibrium is largest. Since the wind speed is higher in spring and fall than in summer, we observe higher carbon fluxes in the western basin compared to the eastern.

The seasonality of the isotopic signature of the air-sea flux is strongly dependent on the CO_2 mass flux. When this reaches 0 while the isotopic disequilibrium stays more or less constant, the isotopic signature of the flux will increase/decrease until infinity. Also, if the CO_2 mass flux changes sign, while the isotopic disequilibrium does not, the isotopic signature of the flux will change its sign. Gas exchange with the atmosphere depletes ^{13}C in the surface ocean CO_2 pool in most regions during summer and fall. Once the CO_2 reservoir gets very light by winter cooling and the ocean is still undersaturated, as in most regions during the winter, the isotope ratio of the flux turns positive and, thus, lightens the pool of inorganic carbon in the surface ocean. Due to the smaller mass flux, the uncertainties are much higher during winter.

The annual CO_2 flux due to air-sea gas exchange (see Figure 5) is slightly increasing in the open ocean from east to west, from (2.62 ± 0.53) mol $CO_2 \cdot m^{-2} \cdot year^{-1}$ to (4.33 ± 0.81) mol $CO_2 \cdot m^{-2} \cdot year^{-1}$, which is in agreement with earlier studies (Lüger et al., 2006; Takahashi et al., 2009) and the long-term mean for this region of 2–3 mol $CO_2 \cdot m^{-2} \cdot year^{-1}$ (Landschützer et al., 2014). On the shelves, the periods of supersaturation cause lower annual fluxes.

The isotope ratio of the annual fluxes is lower in the eastern open ocean than in the western. This is a result of the negative isotopic disequilibrium in these regions during winter. Between 30°W and 40°W, the isotopic disequilibrium was positive all throughout the year. This basic difference is a result of a larger seasonal cycle in the $\delta^{13}C(DIC)$ and thus in the biological driven part of the $\delta^{13}C(CO_2)$ seasonality. The slightly larger peak-to-peak amplitude in the temperature-driven component in the western region did not compensate for that. Another reason could be, that the water masses in the eastern part of the basin are mixed deeper in the east. This leads to higher winter fCO_2 and lower $\delta^{13}C(CO_2)$ toward the east and fits well with the slightly increasing annual flux with an accompanied stronger isotopic signal of the annual flux from 10°W to 45°W.

On the shelves, the isotope ratio of the annual flux was not distinguishable from 0. However, this is not caused by the same reason. On the European shelf, the main driver of very light carbon in the winter is the strong

biological cycle (see Figure 3). In contrast to that, temperature variations play the major role in the Great Bank region. The strong winter cooling reduces the $\delta^{13}C(CO_2)$ in the surface ocean under that of the overlaying atmosphere.

4. Conclusion

We successfully added a CRDS system to an existing autonomous underway fCO_2 system on a voluntary observing ship and can present now a unique 3-year time series of surface water fCO_2 and $\delta^{13}C(CO_2)$. While the use of VOS is established for fCO_2 measurements on different routes in this region, this implementation is new for $\delta^{13}C(CO_2)$. The now available resolution in time and space gives us the possibility to close the data gap in winter and study regional differences in the seasonality of $\delta^{13}C$ of gaseous CO_2 in seawater as well as, calculated from this, the $\delta^{13}C(DIC)$. The direct comparison to the existing $\delta^{13}C(DIC)$ data sets is limited by the calculation of the fraction factor between DIC and gaseous CO_2. As this kind of instruments will most likely be more widely used in the future, we strongly want to encourage to conduct a new estimation of the temperature, salinity, and pH sensitivity of this fractionation factor.

We used this time series to perform a decomposition of the $\delta^{13}C(CO_2)$ seasonality with respect to the driving factors temperature and biology. This decomposition revealed a dominantly biological-driven cycle in the east, while temperature becomes more dominant toward the west. This shift was much clearer in the $\delta^{13}C(CO_2)$ seasonality than in that of fCO_2. Another interesting pattern that could be observed in the western, subtropical part of the basin was the bimodal pattern in $\delta^{13}C(DIC)$ together with a large decrease in DIC concentration. This pattern could be caused by mixing with a subsurface water mass that had experienced an intense bloom. To verify this hypothesis further measurements are needed. Combining the VOS data with a research cruise or floats measuring biogeochemical parameters could help to understand what is going on in the subsurface layer.

In the eastern part of the North Atlantic the seasonal variability of DIC and $\delta^{13}C(DIC)$ is driven by the cycle of primary production in spring and upward mixing of respirational carbon in fall. In the western part the picture is more complicated. Here mixing plays a big role in late summer, reducing the DIC concentration and increasing the $\delta^{13}C(DIC)$. Another process that plays a large role in the western part of the basin during summer is regenerated production. Partial remineralization of particulate organic matter has a potential to be a source of very light carbon to the inorganic carbon pool in oligothroph surface oceans. How large this influence actually is at which time of the season needs further investigation.

In the analysis of the isotopic disequilibrium we could show that the mass and isotopic CO_2 disequilibrium in the North Atlantic surface ocean is almost vanishing during winter. Only in the shelve regions, the surface ocean is lighter than the atmosphere caused by winter cooling and respiratory carbon. During the summer period, the inorganic carbon pool in the surface ocean is in all studied regions heavier than the atmosphere. The overall small isotopic disequilibrium is most likely a cause of the location of the study region at the northern boundary of the subtropical gyre. The sampled surface waters spent a long time in the subtropical gyre in contact with the atmosphere. Once these waters flow northward and cool down, the CO_2 portion of the inorganic carbon is lightening by the temperature-dependent fractionation between DIC and CO_2. The longer equilibration time and the cooling can also be the reason, why the isotope signature of the air-sea flux is smaller in the eastern part than in the west.

This work demonstrates that measuring full seasonal cycles of $\delta^{13}C(CO_2)$ holds a strong potential for understanding the carbon dynamics in the mixed layer. Augmenting the network of data collection and quality control that is already existent for fCO_2 measurements to other continuously measurable parameters, such as $\delta^{13}C(CO_2)$, can significantly improve our understanding of their seasonal and spatial variability. Moreover, the development of precise, autonomous, and low-maintenance instruments for other carbon system or carbon-related parameters, such as nutrients, TA, and organic carbon, and installing them on a VOS could be very useful.

Appendix A : Transects Used in This Study

An overview over the transects during which the data presented in this study was measured can be found in Table A1.

Table A1
Description of the Presented Data Set

Expocode	Period	fCO_2	$\delta^{13}C(CO_2)$	Discrete TA Samples
77CN20120210	February 2012	x		x
77CN20120317	March 2012	x		x
77CN20120525	May/June 2012	x	x	
77CN20120629	July 2012	x	x	x
77CN20120716	July 2012	x	x	
77CN20120730	August 2012	x	x	
77CN20121008	October 2012	x		x
77CN20121026	October/November 2012	x		
77CN20121129	December 2012	x	x	x
77CN20121215	December 2012	x	x	
77CN20130312	February 2013	x	x	x
77CN20130321	March 2013	x	x	x
77CN20130506	May 2013	x	x	x
77CN20130618	June 2013	x	x	x
77CN20130703	July 2013	x	x	
77CN20131004	October 2013	x		x
77CN20131118	November 2013	x		x
77CN20140305	March 2014	x	x	x
77CN20140426	April 2014	x	x	x
77CN20140531	June 2014	x	x	
77CN20140616	June 2014	x	x	x
77CN20140827	August 2014	x	x	x
77CN20140908	September 2014	x	x	
77CN20140928	October 2014	x	x	x
77CN20141102	November 2014	x	x	
77CN20141119	November 2014	x	x	x

Note. TA = total alkalinity.

Acknowledgments
First of all the authors would like to thank the crew, captains, and owner of M/V Atlantic Companion. Without their help and support a work like this would never be possible. We also would like to thank Gernot Friedrichs (University of Kiel, Kiel) for helpful comments and discussions. This work was funded by Project CP1140 of the Future Ocean Excellence Cluster at the University of Kiel. Further substantial support was provided by the European project "CarboChange" (264879) and the ICOS project funded by the German Federal Ministry of Education and Research (01LK1101C, 01LK1224J).The data used are listed in the supporting information.

References

Becker, M., Andersen, N., Fiedler, B., Fietzek, P., Körtzinger, A., Steinhoff, T., & Friedrichs, G. (2012). Using cavity ringdown spectroscopy for continuous monitoring of $\delta^{13}C(CO_2)$ and fCO_2 in the surface ocean. *Limnology and Oceanography: Methods*, *10*(10), 752–766. https://doi.org/10.4319/lom.2012.10.752

Cooperative Global Atmospheric Data Integration Project (2015). *Multi-laboratory compilation of atmospheric carbon dioxide data for the period 1968–2014 obspack_co2_1_globalviewplus_v1.0_2015-07-30*. Boulder, CO: NOAA Earth System Research Laboratory, Global Monitoring Division.

Dickson, A., & Millero, F. (1987). A comparison of the equilibrium constants for the dissociation of carbonic acid in seawater media. *Deep Sea Research Part I: Oceanographic Research Papers*, *34*, 1733–1743. https://doi.org/10.1016/0198-0149(87)90021-5

Dickson, A., Sabine, C., & Christian, J. (2007). *Guide to best practices for ocean CO_2 measurements*, PICES Special Publication 3. Sidney, British Columbia: North Pacific Marine Science Organization.

Frankignoul, C., de Coëtlogon, G., Joyce, T. M., & Dong, S. (2001). Gulf Stream variability and ocean-atmosphere interactions. *Journal of Physical Oceanography*, *31*(12), 3516–3529. https://doi.org/10.1175/1520-0485(2002)

Friedman, I., O'Neil, J., & Cebula, G. (1982). Two new carbonate stable-isotope standards. *Geostandards Newsletter*, *6*(1), 11–12. https://doi.org/10.1111/j.1751-908X.1982.tb00340.x

Friedrichs, G., Bock, J., Temps, F., Fietzek, P., Körtzinger, A., & Wallace, D. W. R. (2010). Toward continuous monitoring of seawater $^{13}CO_2/^{12}CO_2$ isotope ratio and pCO_2: Performance of cavity ringdown spectroscopy and linewidth effects. *Limnology and Oceanography: Methods*, *8*, 523–551. https://doi.org/10.4319/lom.2010.8.539

Gruber, N., Keeling, C. D., Bacastow, R. B., Guenther, P. R., Lueker, T. J., Wahlen, M., & other (1999). Spatiotemporal patterns of carbon-13 in the global surface oceans and the oceanic suess effect. *Global Biogeochemical Cycles*, *13*(2), 307–335. https://doi.org/10.1029/1999GB900019

Gruber, N., Keeling, C. D., & Bates, N. R. (2002). Interannual variability in the North Atlantic Ocean carbon sink. *Science*, *298*(5602), 2374–2378. https://doi.org/10.1126/science.1077077

Johnson, K. M., Dickson, A. G., Eischeid, G., Goyet, C., Guenther, P., Key, R. M., et al. (1998). Coulometric total carbon dioxide analysis for marine studies: Assessment of the quality of total inorganic carbon measurements made during the US Indian Ocean CO_2 Survey 1994–1996. *Marine Chemistry*, *63*(1–2), 21–37. https://doi.org/10.1016/S0304-4203(98)00048-6

Johnson, K., Wills, K., Butler, D., Johnson, W., & Wong, C. (1993). Coulometric total carbon dioxide analysis for marine studies: Maximizing the performance of an automated gas extraction system and coulometric detector. *Marine Chemistry*, *44*(2–4), 167–187. https://doi.org/10.1016/0304-4203(93)90201-X

Khim, B.-K., Otosaka, S., Park, K.-A., & Noriki, S. (2018). $\delta^{13}C$ and $\delta^{15}N$ values of sediment-trap particles in the Japan and Yamato Basins and comparison with the core-top values in the East/Japan Sea. *Ocean Science Journal*, *53*(1), 17–29. https://doi.org/10.1007/s12601-018-0003-5

Körtzinger, A., Quay, P. D., & Sonnerup, R. E. (2003). Relationship between anthropogenic CO_2 and the $^{1}3C$ Suess effect in the North Atlantic Ocean. *Global Biogeochemical Cycles*, *17*(1), 1005. https://doi.org/10.1029/2001GB001427

Körtzinger, A., Send, U., Lampitt, R. S., Hartman, S., Wallace, D. W. R., Karstensen, J., et al. (2008). The seasonal pCO_2 cycle at 49°N/16.5°W in the northeastern Atlantic Ocean and what it tells us about biological productivity. *Journal of Geophysical Research*, *113*, C04020. https://doi.org/10.1029/2007JC004347

Landschützer, P., Gruber, N., Bakker, D. C. E., & Schuster, U. (2014). Recent variability of the global ocean carbon sink. *Global Biogeochemical Cycles*, *28*, 927–949. https://doi.org/10.1002/2014GB004853

Le Quéré, C., Andrew, R. M., Friedlingstein, P., Sitch, S., Pongratz, J., Manning, A. C., et al. (2018). Global carbon budget 2017. *Earth System Science Data*, *10*(1), 405–448. https://doi.org/10.5194/essd-10-405-2018

Lloyd, J., & Farquhar, G. D. (1994). ^{13}C discrimination during CO_2 assimilation by the terrestrial biosphere. *Oecologia*, *99*(3), 201–215. https://doi.org/10.1007/BF00627732

Lüger, H., Wallace, D. W. R., Körtzinger, A., & Nojiri, Y. (2004). The pCO_2 variability in the midlatitude North Atlantic Ocean during a full annual cycle. *Global Biogeochemical Cycles*, *18*, GB3023. https://doi.org/10.1029/2003GB002200

Lüger, H., Wanninkhof, R., Wallace, D. W. R., & Körtzinger, A. (2006). CO_2 fluxes in the subtropical and subarctic North Atlantic based on measurements from a volunteer observing ship. *Journal of Geophysical Research*, *111*, C06024. https://doi.org/10.1029/2005JC003101

Mehrbach, C., Culberson, C., Hawley, J., & Pytkowicz, R. (1973). Measurement of the apparent dissociation constants of carbonic acid in seawater at atmospheric pressure. *Limnology and Oceanography*, *18*, 897–907.

Mintrop, L., Pérez, F. F., González-Dávila, M., Santana-Casiano, M., & Körtzinger, A. (2000). Alkalinity determination by potentiometry: Intercalibration using three different methods. *Ciencias Marinas*, *26*(1), 23–37.

Nightingale, P. D., Malin, G., Law, C. S., Watson, A. J., Liss, P. S., Liddicoat, M. I., et al. (2000). In situ evaluation of air-sea gas exchange parameterizations using novel conservative and volatile tracers. *Global Biogeochemical Cycles*, *14*(1), 373–387.

Olsen, A., Omar, A. M., Bellerby, R. G., Johannessen, T., Ninnemann, U., Brown, K. R., et al. (2006). Magnitude and origin of the anthropogenic CO_2 increase and ^{13}C Suess effect in the nordic seas since 1981. *Global Biogeochemical Cycles*, *20*, GB3027. https://doi.org/10.1029/2005GB002669

Pierrot, D., Neill, C., Sullivan, K., Castle, R., Wanninkhof, R., Lüger, H., et al. (2009). Recommendations for autonomous underway pCO_2 measuring systems and data-reduction routines. *Deep Sea Research Part II: Topical Studies in Oceanography*, *56*, 512–522. https://doi.org/10.1016/j.dsr2.2008.12.005

Quay, P., Sonnerup, R., Munro, D., & Sweeney, C. (2017). Anthropogenic CO_2 accumulation and uptake rates in the Pacific Ocean based on changes in the $^{13}C/^{12}C$ of dissolved inorganic carbon. *Global Biogeochemical Cycles*, *31*, 59–80. https://doi.org/10.1002/2016GB005460

Quay, P. D., Stutsman, J., Feely, R. A., & Juranek, L. W. (2009). Net community production rates across the subtropical and equatorial Pacific Ocean estimated from air-sea $\delta^{13}C$ disequilibrium. *Global Biogeochemical Cycles*, *23*, GB2006. https://doi.org/10.1029/2008GB003193

Quay, P., & Wu, J. (2015). Impact of end-member mixing on depth distributions of $\delta^{13}C$, cadmium and nutrients in the N. Atlantic Ocean. *Deep Sea Research Part II: Topical Studies in Oceanography*, *116*, 107–116. https://doi.org/10.1016/j.dsr2.2014.11.009

Racapé, V., Metzl, N., Pierre, C., Reverdin, G., Quay, P. D., & Olafsdottir, S. R. (2014). The seasonal cycle of $\delta^{13}C_{DIC}$ in the North Atlantic subpolar gyre. *Biogeosciences*, *11*(6), 1683–1692. https://doi.org/10.5194/bg-11-1683-2014

Racapé, V., Pierre, C., Metzl, N., Monaco, C. L., Reverdin, G., Olsen, A., et al. (2013). Anthropogenic carbon changes in the Irminger Basin (1981–2006): Coupling $\delta^{13}C_{DIC}$ and DIC observations. *Journal of Marine Systems*, *126*, 24–32. https://doi.org/10.1016/j.jmarsys.2012.12.005

Steinhoff, T., Friedrich, T., Hartman, S., Oschlies, A., Wallace, D. W., & Körtzinger, A. (2010). Estimating mixed layer nitrate in the North Atlantic Ocean. *Biogeosciences*, *7*, 795–807.

Takahashi, T., Olafsson, J., Goddard, J., Chipman, D., & Sutherland, S. (1993). Seasonal variation of CO_2 and nutrients in the high-latitudesurface oceans: A comparative study. *Global Biogeochemical Cycles*, *7*, 843–878.

Takahashi, T., Sutherland, S. C., Wanninkhof, R., Sweeney, C., Feely, R. A., Chipman, D. W., et al. (2009). Climatological mean and decadal change in surface ocean pCO_2, and net sea-air CO_2 flux over the global oceans. *Deep Sea Research Part II: Topical Studies in Oceanography*, *56*(8–10), 554–577.

van Heuven, S., Pierrot, D., Lewis, E., & Wallace, D. (2009). *MATLAB program developed for CO_2 system calculations*. Oak Ridge, TN: ORNL/CDIAC-105b. Carbon Dioxide Information Analysis Center, Oak Ridge National Laboratory, U.S. Department of Energy.

Wanninkhof, R. (1992). Relationship between wind speed and gas exchange over the ocean. *Journal of Geophysical Research Oceans*, *97*(C5), 7373–7382. https://doi.org/10.1029/92JC00188

Weiss, R. F. (1974). Carbon dioxide in water and seawater: The solubility of a non-ideal gas. *Marine Chemistry*, *2*, 203–215.

White, J., Vaughn, B. H., & Michel, S. (2015). *Stable isotopic composition of atmospheric carbon dioxide (^{13}C and ^{18}O) from the NOAA ESRL Carbon Cycle Cooperative Global Air Sampling Network, 1990–2014, Version: 2015-10-26*. Boulder, CO: University of Colorado, Institute of Arctic and Alpine Research (INSTAAR).

Young, J. N., Bruggeman, J., Rickaby, R. E. M., Erez, J., & Conte, M. (2013). Evidence for changes in carbon isotopic fractionation by phytoplankton between 1960 and 2010. *Global Biogeochemical Cycles*, *27*, 505–515. https://doi.org/10.1002/gbc.20045

Zeng, J., Nojiri, Y., Murphy, P. P., Wong, C., & Fujinuma, Y. (2002). A comparison of ΔpCO_2 distributions in the northern North Pacific using results from a commercial vessel in 1995–1999. *Deep Sea Research Part II: Topical Studies in Oceanography*, *49*(24–25), 5303–5315. https://doi.org/10.1016/S0967-0645(02)00192-3

Zhang, J., Quay, P. D., & Wilbur, D. O. (1995). Carbon isotope fractionation during gas-water exchange and dissolution of CO_2. *Geochimica et Cosmochimica Acta*, *59*, 107–14. https://doi.org/10.1016/0016-7037(95)91550-D